Supporting Information

Structure and Dynamics of Water on Forsterite Surface

Tingting Liu[a*†], Siddharth Gautam[a†], Hsiu-Wen Wang[b], Lawrence M Anovitz[b], Eugene Mamontov[c], Lawrence F Allard[d], and David R Cole[a]

[a]*School of Earth Sciences, The Ohio State University, 125 South Oval Mall, Columbus, OH 43210*

[b]*Chemical Sciences Division, Oak Ridge National Laboratory, Oak Ridge, Tennessee 37831*

[c]*Neutron Scattering Science Division, Oak Ridge National Laboratory, Oak Ridge, Tennessee 37831*

[d]*Materials Science and Technology Division, Oak Ridge National Laboratory, Oak Ridge, Tennessee 37831*

**Corresponding author: Liu.2189@osu.edu*

† *These authors contributed equally to this work.*

Section I. Experimental and MD simulation details

(1) Experiments

Material characterization

Scanning electron microscopy (SEM), transmission electron microscopy (TEM), and X-ray diffraction (XRD) techniques have been applied to characterize the nanoparticle size, morphology, and dominant crystal planes of the synthetic sample. Fig. S1a shows the SEM image where the nanoparticles uniformly show a flaky morphology, and the particle sizes range from 100 ~ 1000 nm. Fig. S1b shows the TEM image of the sample. We can identify the particles are formed in layers and the particle sizes vary from 100 nm to a few ~100 nm. We also endeavored to identify the major crystal plane(s) of the forsterite nanoparticles by TEM; however, the nanoparticles may have not crystallized with dominant planes as shown by the SEM image, the diffraction pattern in TEM did not provide a conclusive result.

Fig. S1c,d show the XRD patterns for the synthetic forsterite sample. Except the mineral phase of forsterite, no other phase is identified. Fig. S1c shows a standard forsterite XRD pattern in which the sample was not processed into nanoparticles. In contrast, Fig. S1d shows a pattern where the (020) peak is significant and broadened compared to the standard pattern. Sample for this pattern underwent further annealing and grinding processes, producing the nanoparticles as shown in Fig. S1a. The prominence and broadening of (020) peak could be due to the preferred orientation of the nanoparticles which mainly exhibit (010) crystal plane as the surface, in accord with the layered feature of the nano-crystal morphology.

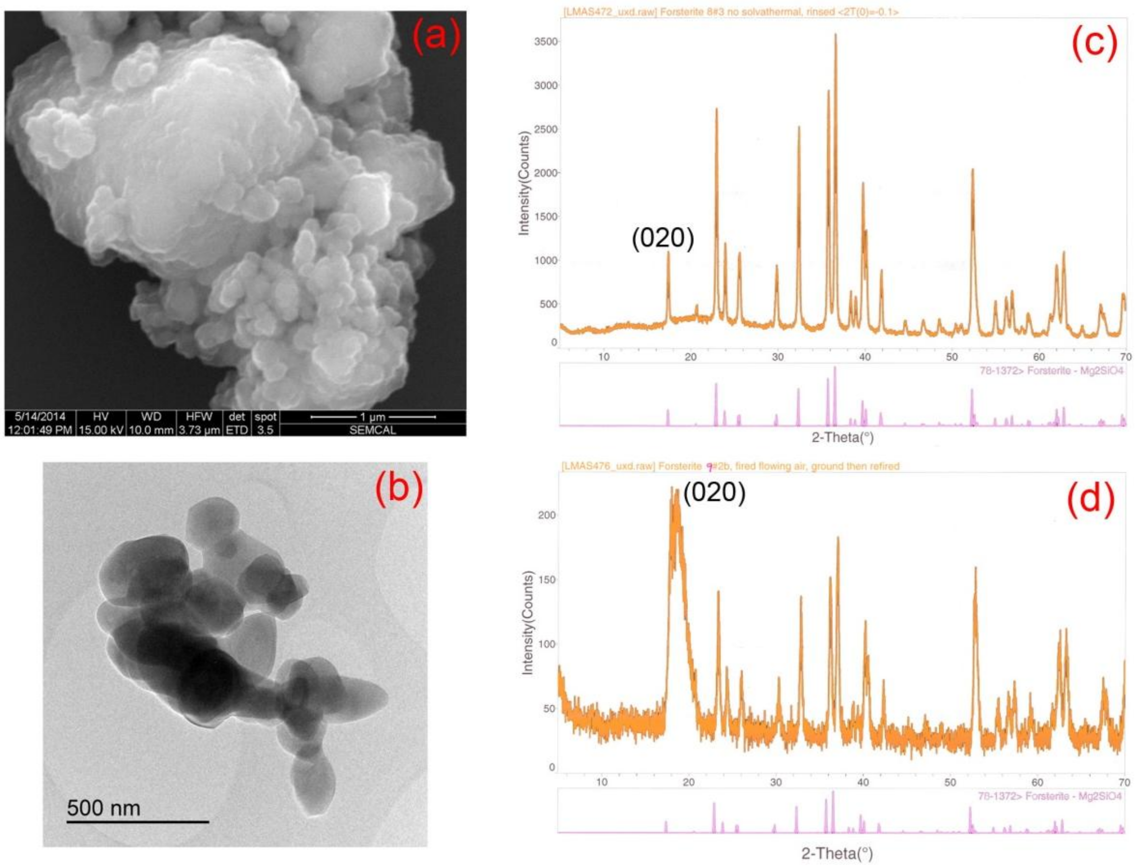

Fig. S1. SEM (a), TEM (b) images, and XRD patterns of a standard sample (c) and a nano-powdered sample (d).

Thermogravimetric analysis (TGA)

Fig. S2 shows the TGA results for hydrated sample that has reached equilibrium with water vapor in vacuum oven. The evacuation in vacuum oven at 50°C could remove part of the physisorbed water on the surface. The results show the water content is ~ 10.0% wt. for fully hydrated surfaces.

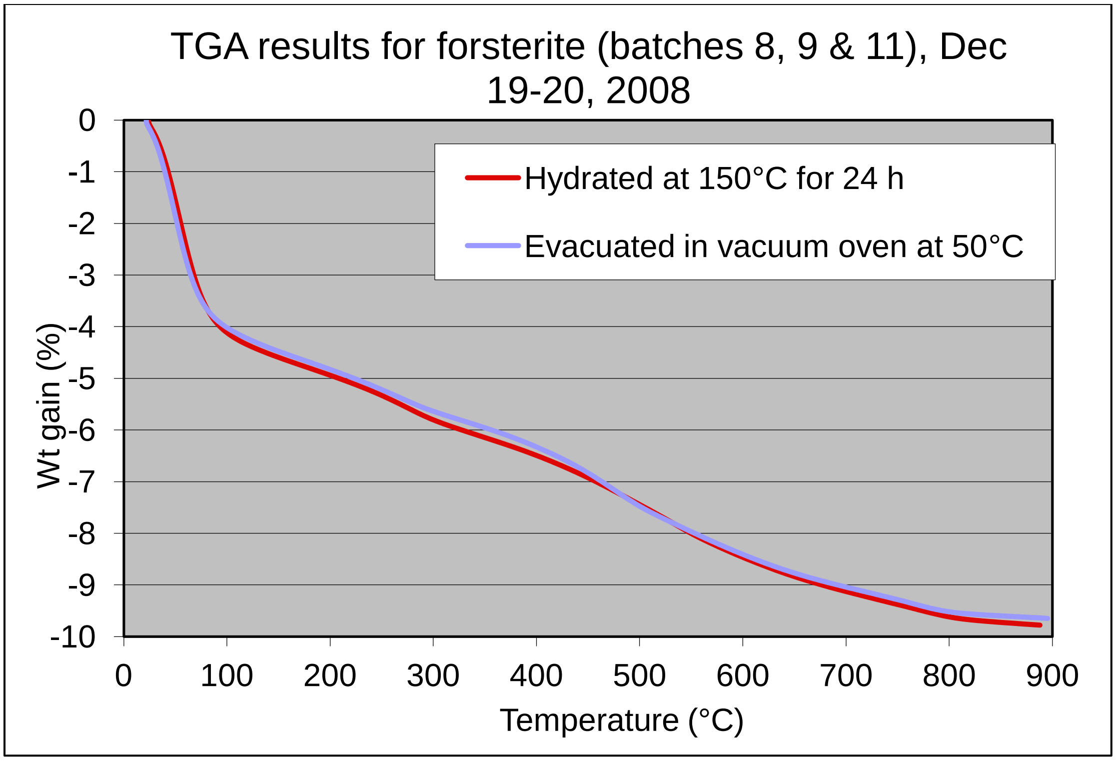

Fig. S2. TGA results using hydrated sample under different pre-treatments.

Time scales probed by the QENS experiments

The time scales accessible by HFBS, DCS, and BASIS are illustrated in Fig. S3, from which we can observe the broad time scales that can be detected in this study and also the time scale overlapping.

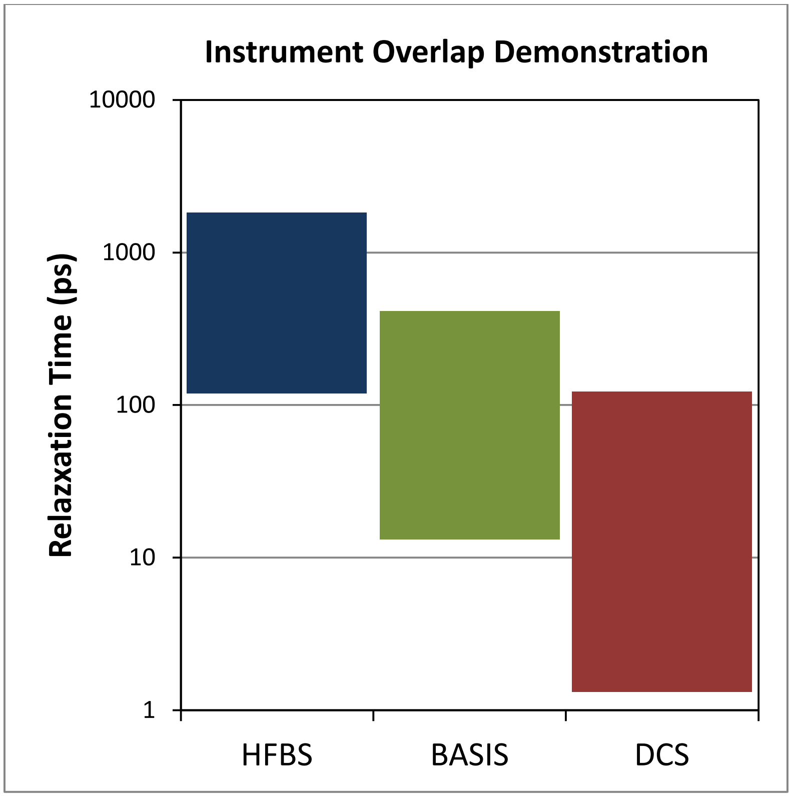

Fig. S3. Time scales accessible by the three QENS instruments.

(2) Simulation details

We adopted the same potential parameters as in Kerisit et al,[1] including the modified CLAYFF model[2] for forsterite and Lennard-Jones interactions. The interaction between Mg and water-oxygen (Ow) is described by Buckingham potentials, which have been used by a number of MgO/water and forsterite/water MD studies.[1,3–5] The two possible forsterite(010) surface terminations are presented in Fig. S4. We chose to hydroxylate on the non-dipolar termination. The hydroxylated surface in this study is decorated by assigning OH groups to every Mg atom on the surface, and H group to the surface oxygen atom (Ox) next to the Mg atom. The charge in forsterite follows Kerisit et al.[1] that is modified from CLAYFF model. In the forsterite slab, Mg=+2.0 e, Si=+2.1 e, O=-1.525 e; while for the Ox, the H binding with Ox, and the O and H atoms of the OH group, their charges are -0.950 *e*, +0.4250 *e*, -1.425 *e*, and +0.4250 *e*, respectively. The SPC/E model for water[6] is used in this study, where the bond length of O-H and bond angle of H-O-H are fixed at the values of 1 Å and 109.47°, respectively. The charges for Ow and Hw atoms are -0.8476 *e* and +0.4238 *e*, respectively. The potential parameters (σ = 3.167 Å; ε = 0.649 $kJ\cdot mol^{-1}$) provided in Heyes[7] yield the closest agreement to experiments on the bulk water diffusion coefficient,[8–10] i.e., a value of 2.39×10^{-9} m^2s^{-1} at 298 K. Details for bulk water simulation is presented below. We have also applied this set of parameters for Ow-Ow to the Ow-related pairs in the simulation. The oscillating mode for OH groups and H groups with surface oxygen atoms is treated as harmonic bond where the parameters follow the SPC water model described in Berendsen et al.[11] A summary of the interatomic potentials is listed in Table S1.

Table S1. Interatomic potential parameters used in this study.

Buckingham potential parameters: $U(r_{ij}) = A \cdot \exp(-\frac{r_{ij}}{\rho}) - \frac{C}{r_{ij}^6}$

Ion pair	A (eV)	ρ (Å)	C (eV·Å^6)
Mg-Ow	60250.0	0.1667	0.00

Lennard-Jones potential parameters: $U(r_{ij}) = (\frac{A}{r_{ij}^{12}}) - (\frac{B}{r_{ij}^6})$, O_H represents the surface oxygen atom that H group connects, whereas O_{HS} represents the oxygen atom from the OH group.

Ion pair	A (eV·Å^{12})	B (eV·Å^6)
Mg-Mg	178.67465	0.00529
Mg-Si	30.09485	0.00259
Mg-O	3666.9838	0.48813
Mg-O_{HS}	2284.35056	0.48813
Mg-O_{HS}	3666.9838	0.48813
Si-Si	3.18413	0.00101
Si-O	295.22024	0.1655264
Si-O_H	295.22024	0.1655264
Si-O_{HS}	295.22024	0.1655264
Si-Ow	295.22024	0.1655264
O-O	27371.6809	27.127707
O-O_H	27371.6809	27.127707
O-O_{HS}	49247.0663	27.127707
O-Ow	49247.0663	27.127707
O_H-O_H	27371.6809	27.127707
O_H-O_{HS}	27371.6809	27.127707
O_H-Ow	30678.5003	27.127707
O_{HS}-O_{HS}	46017.7505	27.127707
O_{HS}-Ow	46017.7505	27.127707
Ow-Ow	27371.6809	27.127707

Fig. S4 shows the side view of forsterite(010) with both the dipolar (dashed line (3)) and the non-dipolar (dashed line (2)) terminations indicated. However, in order to keep the Si-O bond intact, de Leeuw et al. suggested the dipolar termination is at the blue dashed line (3), which is a relatively rough surface.[4] As discussed in the main text of the paper, all the calculations of water adsorption were done using the more stable non-dipolar termination that preserves the $[SiO_4]^{4-}$ tetrahedra.

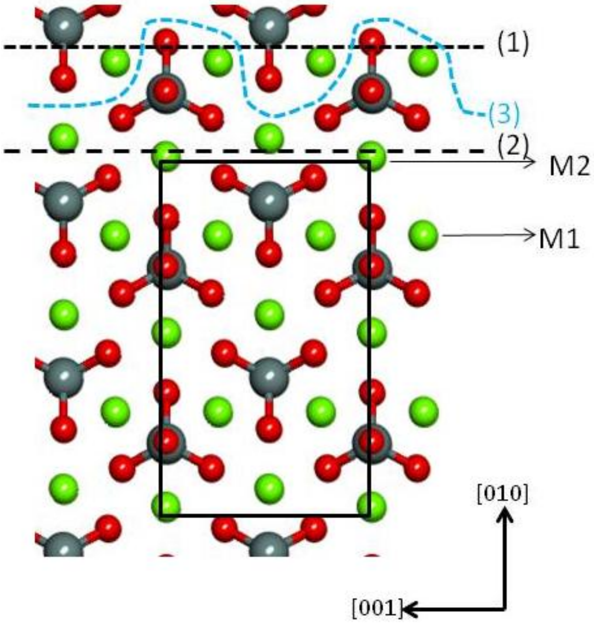

Fig. S4. Side view of forsterite(010) surface. Black frame indicates the size of 1 × 1 unit cell along the [100] direction. Separation at dashed line (2) produces a non-dipolar surface, while line (1) would break Si-O bond. Line (3) indicates the termination of a suggested dipolar surface. M1 and M2 are two Mg atom sites in forsterite. Mg=green spheres, Si=grey spheres, and O=red spheres.

Simulations were conducted at 270 K with NVT ensemble using the Nosé-Hoover thermostat to resemble the experiments. The simulations were set to run for 20 ns. Equilibrium was determined by the variation in the total energy and temperature of the system attaining less than 7% of their constant value. The last 1.5 ns was taken as the production time to calculate average quantities of interest. The Velocity Verlet (VV) algorithm was used to advance the atom positions. Long-range Coulombic energy is estimated using Ewald summation with a precision of 10^{-6}. Smoothed Particle Mesh Ewald (SPME) method developed by Essmann et al[12] is included in DL_POLY_4.06 package. Time step was 1 fs for each step of movement, while the trajectories were recorded at an interval of 0.02 ps. Periodic boundary conditions were applied in all directions. A cutoff distance of 13 Å was used to ensure that there is no interaction between images of water molecules in adjacent cells. The Mg, Si, and O atoms (including O in the OH group) were kept immobile, but the water molecules and the H atoms of the hydroxylated surface were free to move.

(3) Simulation details for bulk water

Bulk water simulation is conducted at 298 K using an NVT ensemble and SPC/E water model.[6] The simulation box is at the length of 21.7 Å in each direction with a total number of 343 water molecules. Thus the density of water in the simulation box is 1.0037 $g \cdot cm^{-3}$. A cutoff distance of 9.3 Å is used. The simulation is set to run 2 ns, and the last 1.5 ns is taken as the production time. Additional calculation algorithms are the same as surface water simulation mentioned above.

(4) How experiment and simulation reach agreement on water content

Using the surface area of the nano-powdered forsterite (66.0 m^2/g) and the cross-sectional area that one molecule takes (0.1 nm^2)[13], one can calculate the number of water molecules per layer per gram of sample. Considering the weight percent of water on the powder's surface (~ 10.0% wt), one can know the total number of water molecules per gram. Therefore, the number of water layers can be estimated, which is ~ 5 - 6 in this study by assuming uniform coverage for the total surface area of the powder. This number of water layers should achieve the full hydration state as stated in the main text that satisfies the immobile L1+L2, and a more mobile L3. In the configuration by MD simulations (Fig. 1 in the main text), the 392 water molecules distribute on both sides of the slab, and both sides generate the three layer structure. Therefore, the hydration scenarios in experiments and simulations are essentially the same.

Section II. More results of QENS and MD

(1) MD simulations

Mean Squared Displacement (MSD)

Mean squared displacements (MSD) in each layer were calculated using the center of mass (COM) trajectories of the molecules that reside continuously in a particular layer for a specific period of duration, e.g., 1.5 ns in L1, 500 ps in L2, and 900 ps in L3. Ten representative molecules from each layer were selected. Fig. S5 shows the overall MSD for all the molecules as well as for molecules residing in certain layers for a period of time, along with the MSD of bulk water calculated in this study for comparison. The diffusion coefficient (*D*) for all the molecules on the surface has been mentioned in the main text, 0.42×10^{-9} m^2s^{-1}, whereas the molecules from L3 yield a *D* value of 0.58×10^{-9} m^2s^{-1}, lower than the *D* of bulk water. The curves for L1 and L2 water indicate that molecules in the two layers are almost immobile.

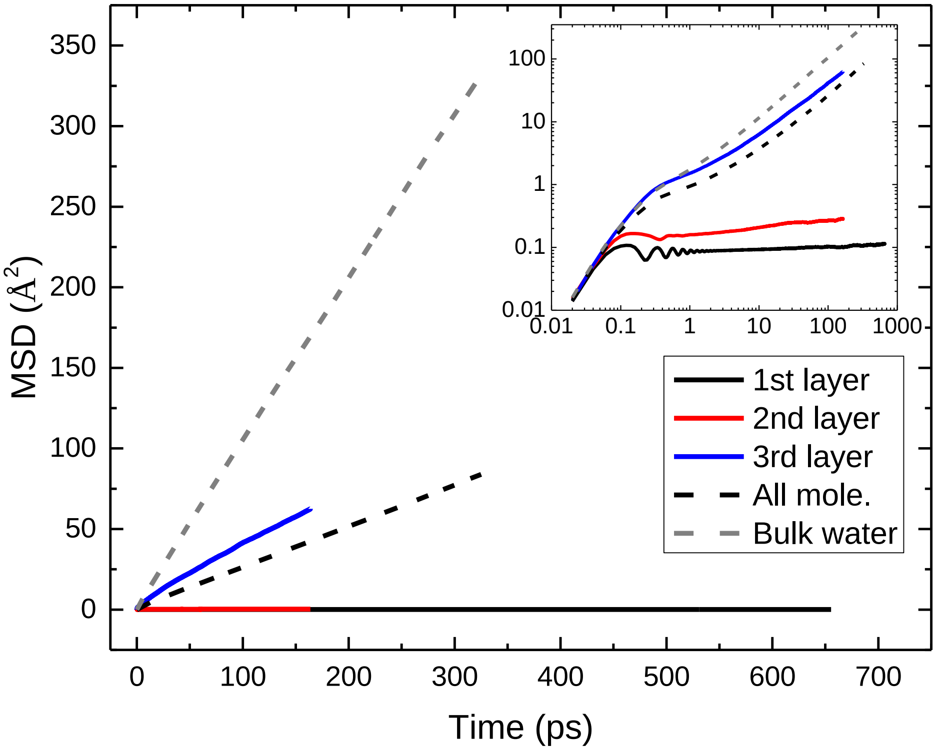

Fig. S5. Calculated MSD of all the 392 water molecules and molecules in different layers, with bulk water for contrast. The inset shows the data in a log-log plot.

Production time of 1.5 ns vs 10 ns

A simulation of 10 ns after equilibration was performed to test if 1.5 ns production time is sufficient, and the total 10 ns was taken as the production time to calculate relevant properties. A longer time interval (0.2 ps) for recording trajectories was adopted to keep the file sizes economical. Note that for production time of 1.5 ns, the time interval was 0.02 ps for recording trajectories. However, for ease of calculation, we used intervals of 0.4 ps and 0.08 ps for calculating MSD and ISF for the above two cases. Fig. S6 shows the comparison for MSD and ISF calculated using 1.5 ns and 10 ns trajectories. We can observe that the properties calculated with 1.5 ns simulation overlap well with those from 10 ns simulation Therefore, 1.5 ns production time is reasonable and sufficient.

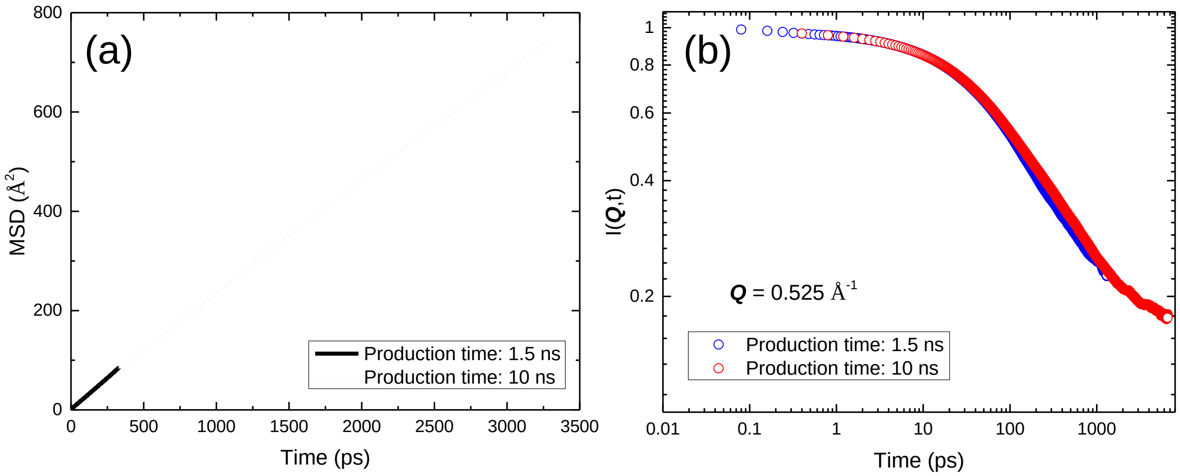

Fig. S6. Production time comparison between 1.5 ns and 10 ns in terms of (a) MSD and (b) ISF at one particular ***Q*** value.

ISF of L3

In Fig. S7, the ISF of L3 (green symbols) is fitted with the following equation,

$$I(Q,t) = A_1 e^{-t/\tau_1} + A_2 e^{-t/\tau_2} + A_3 e^{-t/\tau_3} \tag{S1}$$

where the three time paratmers (τ_1, τ_2, and τ_3) are fixed at the values obtained from the overall ISF fitting using eqn (4) in the main text. Fitting curve and the results are shown in Fig. S7. It can be observed that this attempted fitting matches the ISF of L3. Therefore, we conclude that the overall dynamics is mainly contributed by L3. The coefficients (A_1, A_2, and A_3) indicate the weight percentage of the three exponential components. The value of A_2 (0.60) takes the largest portion compared to A_1 (0.18) and A_3 (0.17). Therefore, the intermediate exponential component (red dashed line) is the major dynamics for surface water molecules .

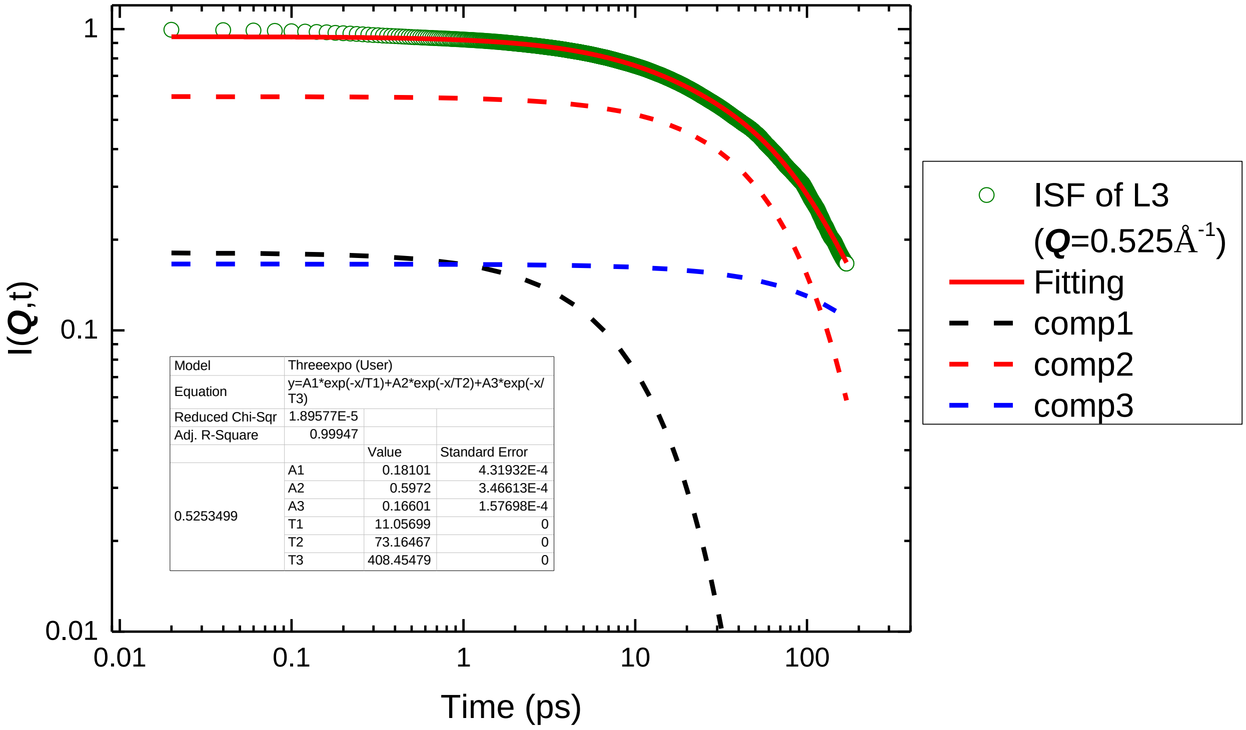

Model	Threeexpo (User)		
Equation	y=A1*exp(-x/T1)+A2*exp(-x/T2)+A3*exp(-x/T3)		
Reduced Chi-Sqr	1.89577E-5		
Adj. R-Square	0.99947		
		Value	Standard Error
0.5253499	A1	0.18101	4.31932E-4
	A2	0.5972	3.46613E-4
	A3	0.16601	1.57698E-4
	T1	11.05699	0
	T2	73.16467	0
	T3	408.45479	0

Fig. S7. ISF of water in L3 at the ***Q*** value of 0.525 Å^{-1}. Three exponential components are plotted in dashed lines.

Rotational properties

Dynamical properties can be divided into translation and rotation. The separation of the two types of motions can be facilitated by separating the coordinates in different frames of reference. For example, one can decompose the position vector of an atom in space fixed frame into center of mass coordinates and coordinates with respect to center of mass, such that:

$$\boldsymbol{r}_0 = \boldsymbol{r}_{CM} + \boldsymbol{d} \tag{S2}$$

where $\boldsymbol{r}_0$ represent the coordinates of an atom constituting the molecule in the space fixed frame of reference, $\boldsymbol{r}_{\mathrm{CM}}$ represent the space fixed coordinates of center of mass of the molecule, and $\boldsymbol{d}$ represent the coordinates of this interaction site in center of mass frame. Their spatial relationship is illustrated in Fig. S8 using water molecule as an example.

The translational motion can be obtained by analyzing the space fixed center of mass coordinates of the molecules ($\boldsymbol{r}_{\mathrm{CM}}$), and the rotational motion analysis uses the coordinates of the constituent atoms in the center of mass frame ($\boldsymbol{d}$).[14] Fig. S8b shows the coordinate relationship of hydrogen atoms whose coordinates in the space fixed frame ($\boldsymbol{r}_{\mathrm{H}}$) were used to analyze the intermediate scattering function (ISF) including translation and rotation, i.e.,

$$r_{H_1} = r_{CM} + r_{H_1}^{CM}, \text{ and } r_{H_2} = r_{CM} + r_{H_2}^{CM} \tag{S3}$$

The space fixed center of mass coordinates ($\boldsymbol{r}_{\mathrm{CM}}$) have been used to analyze the mean squared displacement (MSD) as discussed earlier and plotted in Fig. S5.

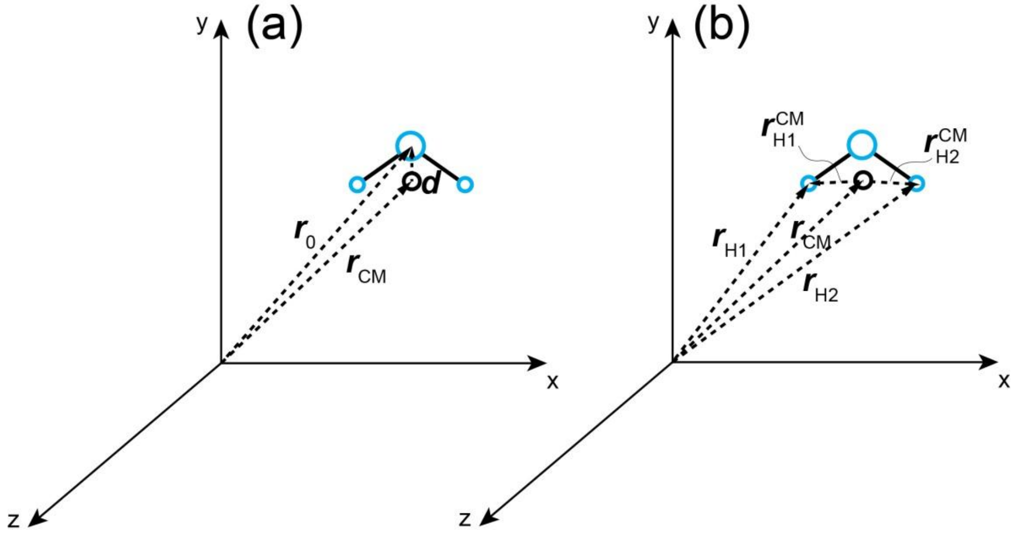

Fig. S8. (a) An illustration of water molecule in fixed space, where $\boldsymbol{r}_0$ represents the coordinates of the Ow atom, and the black circle represents the center of mass of the molecule. (b) An illustration of vector relationship for hydrogen atoms.

Rotational ISF

Rotational ISF (RISF) represents the temporal and spatial information of rotational motion. Fig. S9 shows the RISF curves for eight $\boldsymbol{Q}$ values at 270 K. Instead of coordinates of atom in the center of mass frame ($\boldsymbol{d}$), a unit vector $\boldsymbol{u}$ is used to produce the RISF curves using eqn (3) in the main text, with $\boldsymbol{r}$ replaced by $\boldsymbol{u}$. As seen in Fig. S9, the RISF data undergo three decay stages. The fast decay lasts for ~ 0.2 ps, followed by a slower decay ending at ~ 5 ps, and the slowest decay after 5 ps. The three stages of decay indicate different time scales of the rotational motion, which was also observed for water molecules in the interlayers of clay minerals.[15] The very fast rotational motion below ~ 0.2 ps corresponds to a quasi-elastic width of ~ 3.29 meV, which would appear as a flat background due to its broadness in the quasi-elastic spectra obtained from HFBS, DCS and BASIS. By fitting the second and the third stages (after 0.2 ps) using

$$I_R(Q,t) = A_1 \cdot e^{-t/\tau_1} + A_2 \cdot e^{-t/\tau_2} + c \tag{S4}$$

we obtained the time parameters (τ_1^R , τ_2^R) equal to ~ 6 ps and ~ 45 ps, which correspond to 109.7 μeV and 16.5 μeV (HWHM) in energy scale, respectively. This is well within the detected energy scales accessible by DCS and BASIS if referred to Fig. 4 in the main text. The time parameter (τ_i^R) obtained for each ***Q*** value is similar due to the nature of rotational motion which implies a ***Q*** independent time scale.

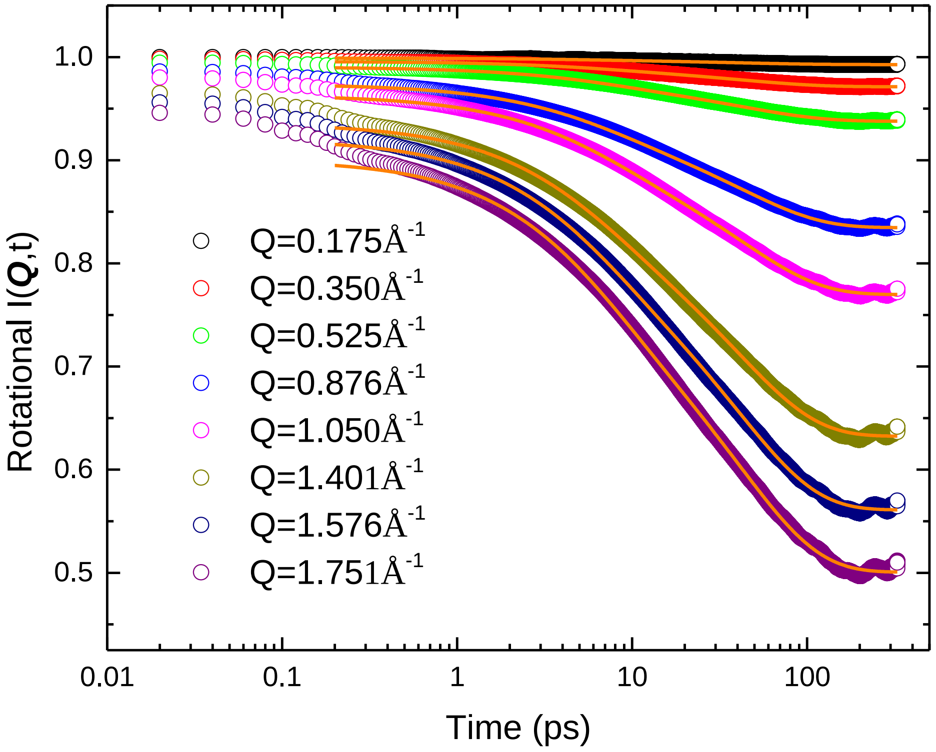

Fig. S9. Calculated rotational ISF data for eight ***Q*** values at 270 K. Orange lines are the fitting curves using eqn (S4).

Residence time (τ_R)

The residence autocorrelation function (RACF) is used to quantify the average time of a molecule residing in certain regions, i.e., residence time. For a given region of space *i*, the RACF for that region, ($R_i(t)$) can be calculated as[16,17]

$$R_i(t) = \frac{\left\langle \theta_i(0) \cdot \theta_i(t) \right\rangle}{\left\langle \theta_i^2(0) \right\rangle} \tag{S5}$$

where $\theta_i(t)$ is a Heaviside step function that takes the value of 1 if a molecule is in the given region *i* at time *t* and all previous times; otherwise 0 if the molecule is outside the region. Triangular brackets denote ensemble average. Here we used this function to present an observation for water molecules in three different layers at 270 K. The defined regions for each layer is according to their positions shown in Fig. 1b in the main text. Fig. S10 shows the R_i(t) function for water molecules in the three layers. Average residence times were estimated by fitting the RACF curves with single exponential decay functions.[16] The derived average residence times are 956 ps, 49.5 ps, and 335 ps for L1, L2, and L3, respectively. It is expected that molecules in L1 has a longer residence time whose typical trajectory can be observed in Fig. 1d. The reason why molecules in L3 stays longer than those in L2 is due to the larger geometrical thickness of L3.

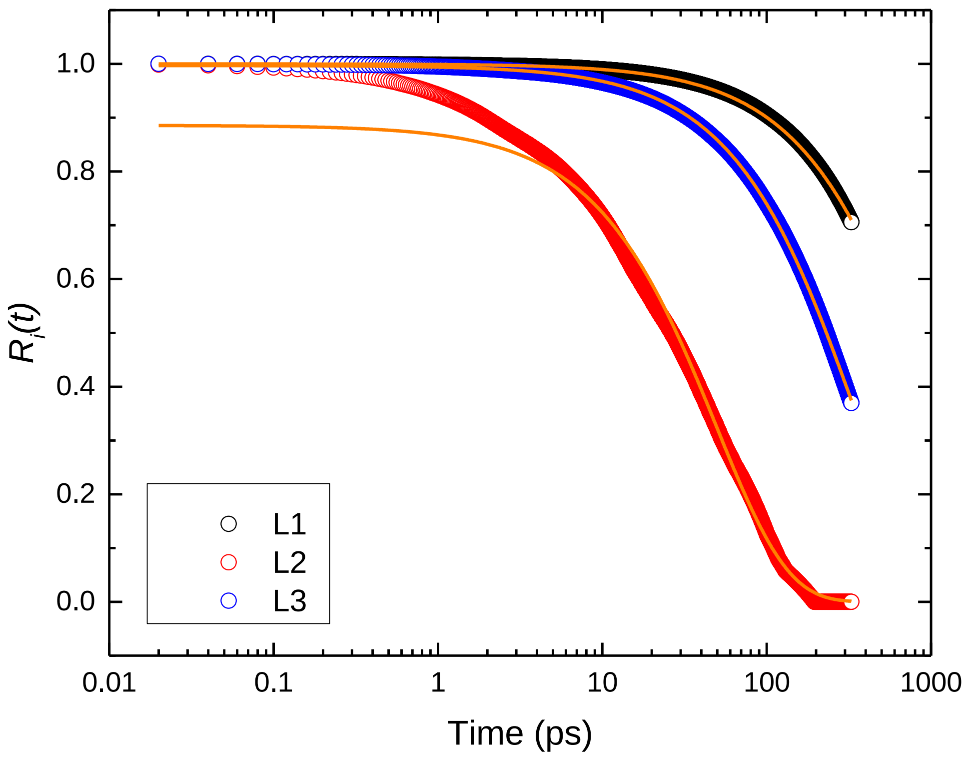

Fig. S10. Normalized residence autocorrelation function of water molecules in different layers on hydroxylated forsterite(010) surface at 270 K.

(2) QENS experiments

QENS data fitting also generates the elastic incoherent structure factor (EISF) which is $A(\boldsymbol{Q})$ in eqn (2) in the main text, and prefactor (p) that weighs the broadening contribution of the two components. Fig. S11a plots the corresponding EISF values determined by QENS data fitting, whereas Fig. S11b shows the prefactor from BASIS and DCS. As only one Lorentzian function is used for HFBS data fitting, there is no prefactor from HFBS.

In Fig. S11a, the EISF data from DCS shows a $\boldsymbol{Q}$-dependence, and data from BASIS shows a smooth $\boldsymbol{Q}$ variation overlapping with the DCS data at low $\boldsymbol{Q}$ values, but data from HFBS do not show much variation. It can be inferred that localized motions are well observed by BASIS and DCS. This is consistent with the finding from the simulations that rotational motions can be expected to contribute to the DCS and BASIS spectra. However, in presence of two different populations of molecules contributing to the broadening of the DCS and BASIS spectra, it is difficult to attribute the EISF variation to a standard model of rotational motion. In Fig. S11b, the prefactors uniformly increase with $\boldsymbol{Q}$ value increasing. Based on eqn (2) in the main text, p is the prefactor of Lorentizan component $L_1(\Gamma_1,\omega)$, and (1 - p) is the prefactor of Lorentzian component $L_2(\Gamma_2,\omega)$. Our fitting results for QENS experiments show that $L_1(\Gamma_1,\omega)$ is faster for both DCS and BASIS compared to $L_2(\Gamma_2,\omega)$. The greater the prefactor, the more contribution to the broadening from one of the two Lorentzians that corresponds to the prefactor. Therefore, in Fig. S11b, it indicates that the fast component which is represented by p (> 0.5) makes more contribution in BASIS; while the slow component which is represented by (1 - p) (>0.5) makes more contribution in DCS. As illustrated in the main text, the BASIS-fast and DCS-slow components and the intermediate calculated component Γ_2^s are the primary contributors for the dynamics. Here using the fitted parameter of p, we proved again the dominant components derived from QENS experiments.

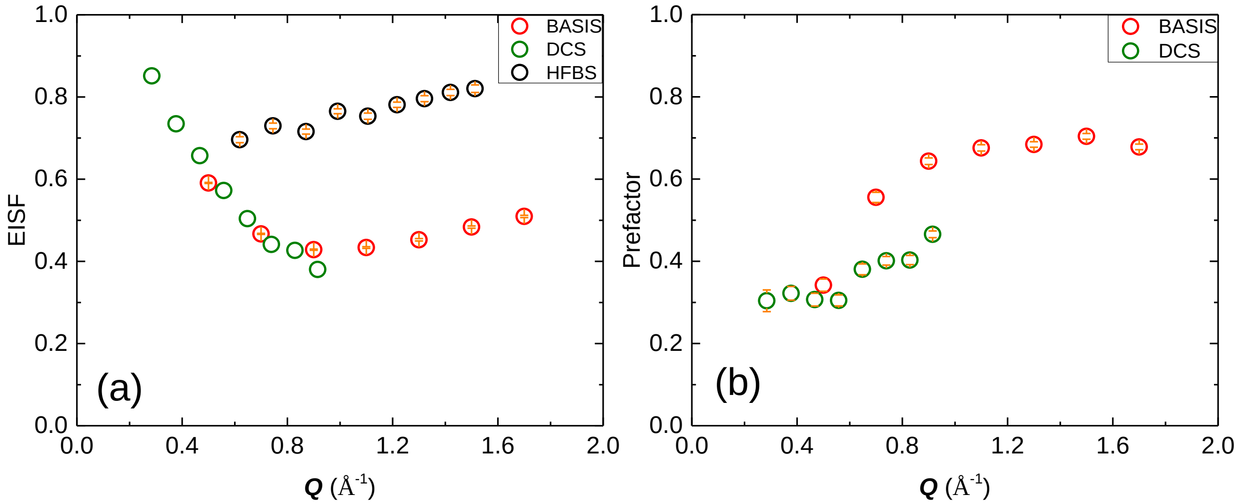

Fig. S11. (a) Fitted EISF comparison between three instruments (BASIS, DCS, HFBS), (b) Fitted prefactor comparison between BASIS and DCS.

In Fig. S12, the fast and slow components determined by BASIS at 270, 285, and 300 K are compared. It can be observed that although temperature is a factor influencing the dynamics where the dynamics at 270 K is the slowest; data from three temperatures show the same trend and the difference between 270 K and 300 K is approximately by a factor of 1.5.

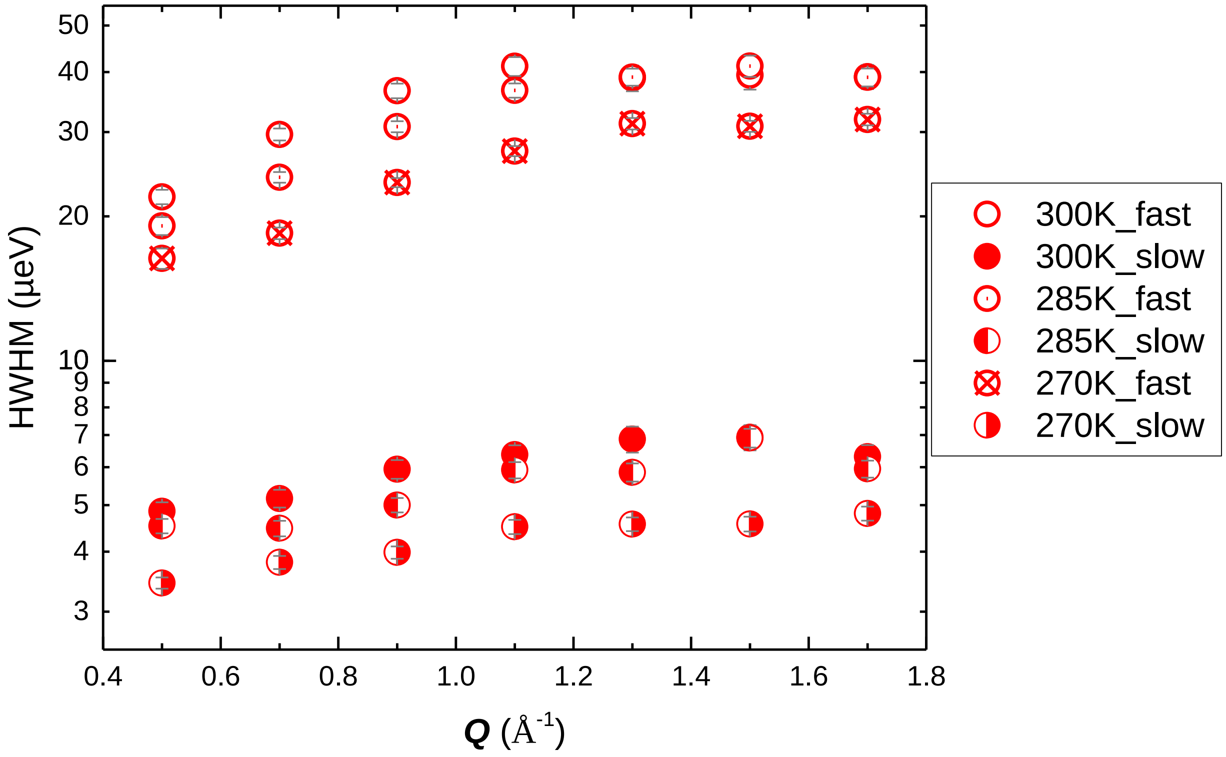

Fig. S12. Fast and slow components determined by BASIS at 270, 285, and 300 K. Grey lines indicate the error bar.

References

1 S. Kerisit, J. H. Weare and A. R. Felmy, Structure and dynamics of forsterite–scCO2/H2O interfaces as a function of water content, *Geochim. Cosmochim. Acta*, 2012, **84**, 137–151.

2 R. T. Cygan, J. Liang and A. G. Kalinichev, Molecular Models of Hydroxide , Oxyhydroxide , and Clay Phases and the Development of a General Force Field, *J. Phys. Chem. B*, 2004, **108**, 1255–1266.

3 H. E. King, M. Stimpfl, P. Deymier, M. J. Drake, C. R. A. Catlow, A. Putnis and N. H. de Leeuw, Computer simulations of water interactions with low-coordinated forsterite surface sites: Implications for the origin of water in the inner solar system, *Earth Planet. Sci. Lett.*, 2010, **300**,

11–18.

4 N. H. de Leeuw, S. C. Parker, C. R. a. Catlow and G. D. Price, Modelling the effect of water on the surface structure and stability of forsterite, *Phys. Chem. Miner.*, 2000, **27**, 332–341.

5 N. H. de Leeuw and S. C. Parker, Molecular-dynamics simulation of MgO surfaces in liquid water using a shell-model potential for water, *Phys. Rev. B*, 1998, **58**, 13901–13908.

6 H. J. C. Berendsen, J. R. Grigera and T. P. Straatsma, The Missing Term in Effective Pair Potentialst, *J. Phys. Chem.*, 1987, **91**, 6269–6271.

7 D. M. Heyes, Physical Properties of Liquid Water by Molecular Dynamics Simulations, *J. Chem. Soc. Faraday Trans*, 1994, **90**, 3039–3049.

8 A. J. Easteal, W. E. Price and L. A. Woolf, Diaphragm Cell for High-temperature Diffusion Measurements, *J. Chem. Soc. Faraday Trans*, 1989, **85**, 1091–1097.

9 M. Holz, S. R. Heil and A. Sacco, Temperature-dependent self-diffusion coefficients of water and six selected molecular liquids for calibration in accurate 1H NMR PFG measurements, *Phys. Chem. Chem. Phys.*, 2000, **2**, 4740–4742.

10 K. Krynicki, C. D. Green and D. W. Sawyer, Pressure and temperature dependence of self-diffusion in water, *Faraday Discuss. Chem. Soc.*, 1978, **66**, 199–208.

11 H. J. C. Berendsen, J. P. M. Postma, W. F. Van Gunsteren and J. Hermans, in *Reidel Publ. Co., Dordrecht*, 1981, pp. 331–342.

12 U. Essmann, L. Perera, M. L. Berkowitz, T. Darden, H. Lee and L. G. Pedersen, A smooth particle mesh Ewald method, *J. Chem. Phys.*, 1995, **103**, 8577–8593.

13 S. Chen and A. Navrotsky, Calorimetric study of the surface energy of forsterite, *Am. Mineral.*, 2009, **95**, 112–117.

14 S. Gautam, Use of quasielastic neutron scattering and molecular dynamics similation to study molecular dynamics under confinement, *Horizons World Phys.*, 2017, **290**, 25–44.

15 L. J. Michot, A. Delville, B. Humbert, M. Plazanet and P. Levitz, Diffusion of Water in a Synthetic Clay with Tetrahedral Charges by Combined Neutron Time-of-Flight Measurements and Molecular Dynamics Simulations, *J. Phys. Chem. C*, 2007, **111**, 9818–9831.

16 S. Kerisit, E. S. Ilton and S. C. Parker, Molecular Dynamics Simulations of Electrolyte Solutions at the (100) Goethite Surface, *J. Phys. Chem. B*, 2006, **110**, 20491–20501.

17 U. Terranova and N. H. de Leeuw, Structure and dynamics of water at the mackinawite (001) surface, *J. Chem. Phys.*, 2016, **144**, 094706.